The Mesicopter: A Meso-Scale Flight Vehicle
NIAC Phase I Final Report

1. Abstract

The following report summarizes the findings of a six month research investigation of the 'mesicopter' concept, a flying vehicle with dimensions of about two and a half centimeters. Research focused on low Reynolds number aerodynamics, motor and power system design, and meso scale fabrication methods.

Our work resulted in the design, component fabrication, and assembly of two mesicopter prototypes. The first version, a 4-motor design with 1.5 cm rotor diameters, externally powered, and mounted on a constrained arm, was used to demonstrate lift off. Each motor was able to lift over 700mg, more than enough to support the weight of the 325mg motor-rotor assembly and leaving sufficient room to carry airframe and battery. A second design shows batteries and airframe integrated into a single structure, free flight tests of this vehicle are envisioned in the near future.

The present work established a methodology for the fabrication of fully 3D shaped propeller blades less than 100 micron thin and with surface roughness of less than one micron. Simulations and measuments indicate the critical importance of blade shape details for aerodynamic performance.
Finally, studies of currently available battery technology revealed that a free flight mesicopter with missions times of tens of minutes is feasible. The prospect of fabricating large number of mesicopters has implications for several future NASA missions.

2. Introduction

The science of flight of millimeter and centimeter size vehicles is largely unexplored. The Reynolds number of such devices lies in the range of less than 10,000 where aerodynamics are dominated by viscous considerations and few analysis or design tools are available. This is one of the areas in which scaling laws are unfavorable, with lower lift-to-drag ratios and limited rotor lift capabilities. Some of the aerodynamic features are poorly understood in this size regime and means by which improved performance may be realized have been little explored. In an effort to shed further light on insect scale aerodynamics, faculty and students from the Aero/Astro Department and the Mechanical Engineering Department at Stanford University with support from NASA embarked on a half year study towards assessing the feasibility of creating a centimeter sized flying vehicle called the 'mesicopter.' Vehicles in this size range may be used on earth for atmospheric science, permitting in-situ measurements of meteorological phenomena such as downbursts and wind shear, and on planets like Mars where atmospheric flight permits unique opportunities for exploration. Swarms of mesicopters could provide atmospheric scientists with information not obtainable using current techniques and could aid in the understanding of phenomena that play a critical role in aviation safety. Better characterization of atmospheric phenomena on Mars and other simple sensing tasks may be feasible with these very low mass and low cost aerial micro-robots. The mesicopter has the potential to pioneer the application of new aerodynamic design concepts and novel fabrication techniques. The objectives for the first six months in this program included determining whether creating a centimeter size flight vehicle is possible at all. The development of appropriate design and fabrication methods suitable for this class of vehicle was the first logical step towards realizing the mesicopter.

3. Phase I Accomplishments

The first phase of the current research program was aimed at determining whether powered flight at these scales was feasible. The work included computational and experimental aerodynamic analyses, motor and power system design, and development of meso-scale fabrication methods. Our efforts resulted in the design, component fabrication, and assembly of two mesicopter prototypes. These 4-motor designs with 1.5 cm rotor diameters are shown in figures 1 and 2. The first version was externally powered and tested on a constrained arm to establish positive net thrust and to avoid instabilities due to thrust differences in any of the four motors. The second design illustrates how batteries might be housed on-board and will be tested and flown on its own power.

Figure 1: Mesicopter with external power supply

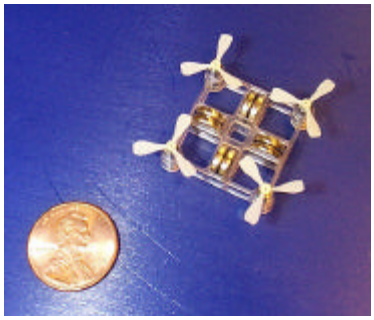

Figure 2: Battery powered mesicopter

3.1 Basic Scaling Issues, System Concepts and Applications

Initial work in Phase I focussed on developing scaling relationships for subsystem weights and aerodynamic performance to ascertain the limits to rotorcraft dimensions and to correlate the performance possibilities with potential applications. This began with a survey of available motor and battery technology and a simplified analysis of optimal rotors over a large range of scales.

Texts on rotor aerodynamics come to different conclusions regarding the scaling of rotor performance with size, depending on the selected constraints. In most references rotor tip speed is fixed and simplifying assumptions about optimal loading and chord distributions are made. These simplifications are reasonable for large scale systems, but which lead to incorrect scaling at the dimensions of interest here. A recent paper [1] did address very small, externally powered rotors, but included simplistic aerodynamic analyses and rotors designed to lift only their own weight. Scaling laws derived in this reference are not appropriate for the systems envisioned here, which motivated new analysis and optimization.

Data from these studies is included in subsequent sections of this report, but the basic conclusion was that systems of the scale we originally contemplated (with 1cm to 10cm rotors) would be feasible. Using commercially-available brushless DC motors and current-technology battery systems, we could build a 3g mesicopter with four 1.5 cm rotors that should be able to lift itself and fly for 30 minutes on earth. With reduced endurance the device would be capable of lifting a 1g payload. With improved battery technology or with motors better matched to the optimal rotor

speeds we could increase the endurance and payload capability substantially. If the overall device size and weight are increased, larger payloads more compatible with existing and near-term technology can be carried. We considered payloads of 1, 10, and 50g to determine the trade-offs between vehicle size and endurance. We also considered flight on Mars where the atmospheric density is just 1% of the sea level earth value. This requires larger rotors for a given system weight, but with reasonable assumptions for battery technology we concluded that mesicopters with these payloads were feasible for Mars applications as well. The specific mission scenarios are discussed briefly in our proposal, and are currently under discussion with NASA and JPL researchers.

The first phase of this work focussed on improving these assessments, developing design tools and concepts, and demonstrating some of the technologies that would be needed for successful realization of the idea. During Phase II we would further develop the design concept based on more specific mission scenarios, but our goal in Phase I was to show that a vehicle could indeed be designed to fly at this scale.

3.2 Aerodynamics

The operating regime of the mesi-scale helicopter poses certain difficulties for aerodynamic analysis and design. Current sizing and motor parameters result in a rotor tip Reynolds number of approximately 5000. It is unclear to what extent classical airfoil and finite wing analysis and design methods are applicable in this flow regime. The highly viscous nature of the flow field, large increases in the boundary layer thickness, and the potential for large regions of separated flow, all create the potential for large discrepancies in performance from what might be expected from experience at higher Reynolds numbers.

Very little experimental or computation work exists to date for aerodynamic lifting surfaces operating at such low Reynolds numbers. Much of the work completed thus far under the current program has gone towards a comparison of the analysis tools currently available, investigation of the unique characteristics of two-dimensional airfoils operating in this regime, and the assessment of the potential performance benefits of detailed section and planform design. The last point is of particular interest for it forms a strong motive and basis for future research and provides insight into the complexity and depth of the available design space.

3.2.1 Simple Rotor Scaling Study

Work began with basic performance estimation using analytical models of rotor performance. A conventional combination momentum theory and blade-element theory leads to spreadsheet-level trades that illustrate mesicopter induced and profile power requirements. In conjunction with payload, battery, and motor weight estimates, a rapid calculation of vehicle power and endurance is obtained. The results of this preliminary study suggested that with commercially-available motors and modern primary battery technology, mesicopters with centimeter-scale rotors could be designecd to stay aloft for as long as 30 minutes. Discussions with NASA researchers prompted looks at vehicles that could fly on Mars and carry small (up to 10g) imaging payloads. With more advanced battery technology and somewhat smaller disk loadings than would be used on Earth, we developed preliminary designs for these vehicles.

3.2.2 Refined Computational Tools

Current computational analysis tools fit into two categories, full viscous flow field solvers working with some formulation of the Navier-Stokes equations, and methods that divide the flow field into an outer inviscid flow region and a viscous boundary layer. Two different Navier-Stokes codes have been examined for application to this work. The first is the FLO103 code [1], a RANS solver for the full Navier-Stokes equations. This solver was not intended for low Mach number and ultra low Reynolds number analysis and has had very limited success in this current application. Fully laminar converged solutions have been obtained for Mach Numbers as low as 0.3 and Reynolds numbers as low as 20,000, but this is still significantly out of the current operating regime. Further improvements in convergence may be possible through careful grid refinement, but this tool appears to be only marginally applicable to this problem. It is important to note that this is not a shortcoming of this particular code, but of this type of flow solver in general.

The second Navier-Stokes solver considered is the INS2D code, developed by Stuart Rogers at NASA Ames [2]. This code solves an incompressible formulation of the Navier-Stokes equations. It is much better suited to analysis at ultra-low Reynolds numbers and has been used for the majority of two-dimensional section analysis to date. Figure 3 illustrates one of the solutions from this code. Note the thick wake that necessitates the use of Navier-Stokes methods.

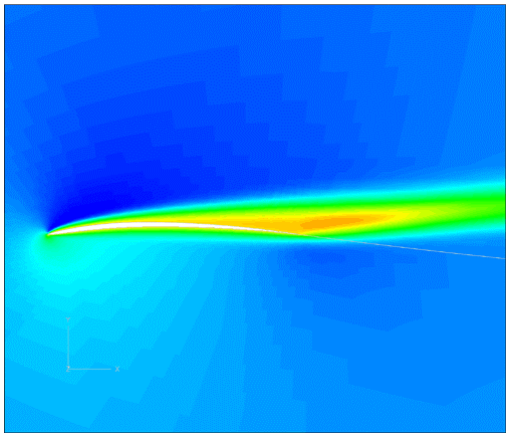

Figure 3. INS2D Solution: Contours of pressure showing thick viscous wake.

The inner/outer flow field methods available solve the outer flow field using either a potential flow formulation via a classical panel method, or by solving the Euler equations for inviscid, compressible flow. The viscous boundary layer solution is generally some variant of an integral formulation of the Prantdl boundary layer equations.

One inner/outer flow field code that has been implemented, with limited success, is the MSES program developed by Mark Drela at MIT [3]. This is a two-dimensional Euler solver coupled with an integral boundary layer formulation. It appears to give reasonable drag predictions over a narrow range of angle of attack, but the limitations of the boundary layer formulation cause the solution to diverge if substantial regions of separated flow exist. Unfortunately, this is often the case with these airfoils at even moderate angles of attack.

The much simpler and faster panel methods can be unsuited for analyzing very thin sections, below 1% to 2% thick. Depending on the implementation of the surface boundary conditions and the types

and placement of singularity elements, the resulting linear system may become nearly singular. The current section thickness is approximately 2% thick due to manufacturing constraints. This does allow for limited analysis using any of the commonly available airfoil design and analysis codes such as Xfoil [4] or the Eppler code [5]. These codes face the same severe angle of attack limitations as MSES, since all share similar boundary layer formulations. For incompressible flows with adequate section thickness, panel methods are faster and appear to be considerably more robust. For very thin sections or higher Mach numbers, MSES would be more applicable.

3.2.3 Comparison of MSES and INS2D Solutions

MSES and INS2D fully laminar, steady-state solutions have been compared for two airfoils at a Re 1000. The airfoils sections are the NACA 4402 and 4404 profiles. The resulting lift curve and drag polar plots are provided in Figure 4 and Figure 5. Each data set is complete up to the point at which a given code failed to converge.

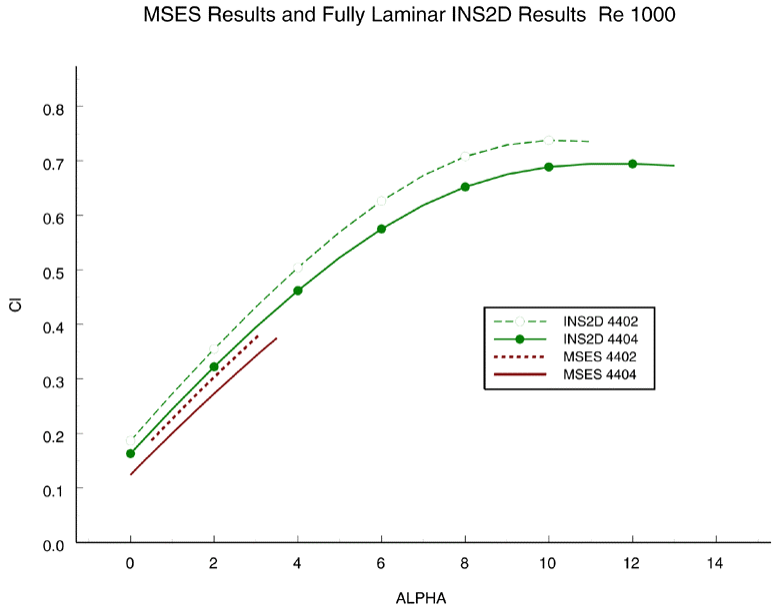

Figure 4. Variation of lift coefficient with angle of attack from INS2D and MSES.

Several trends are apparent from the figures. The most obvious is that MSES fails to converge significantly earlier than the INS2D code, reaching only 50% of the INS2D predicted C_{lmax} . The angle of attack at which it fails roughly corresponds to the development of substantial stable eddy regions along the upper surface in the INS2D solution. The coupled Euler and integral boundary layer formulation has only limited capability to deal with laminar separation bubbles and small regions of separation. The INS2D solution continues to converge past C_{lmax} until the behavior of the flow field becomes unsteady at high angles of attack. There is the capability to run the INS2D code for an unsteady, time varying solution. This would likely be incorporated into future work.

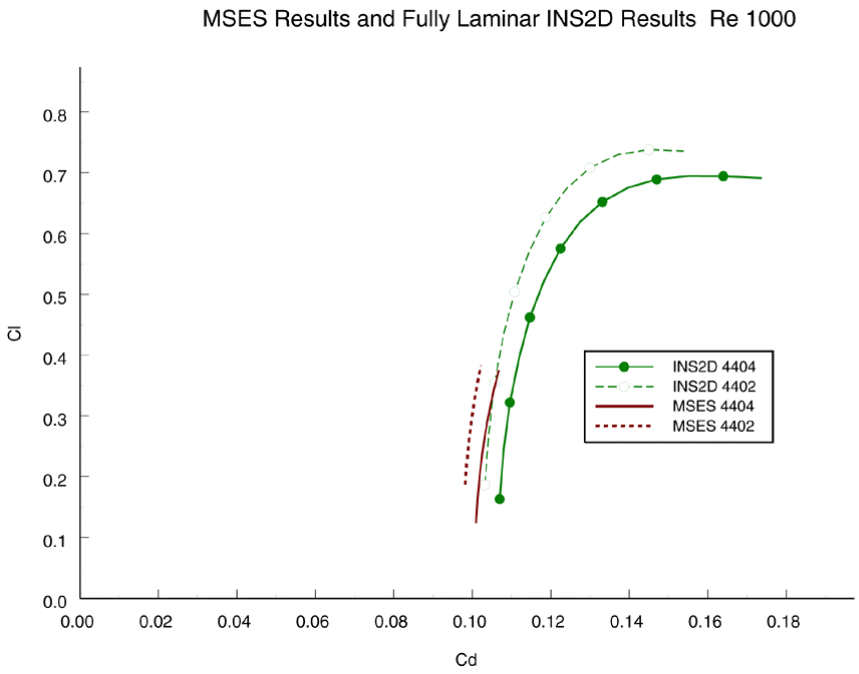

Figure 5. Variation of drag coefficient with lift from INS2D and MSES.

The other visible trends are consistent shifts in both the lift curve plots and the drag polars. The is a 0.05 constant shift in the lift coefficient corresponding to a 15% to 25% variation between the two solutions. The constant shift in drag for a fixed lift is approximately 50 counts, corresponding to a 5% shift in Cd_o .

This variation can be partially attributed to the governing equations of the integral boundary layer formulation. The Prandtl boundary layer equations assumes pressure is constant along the perpendicular from the surface to the edge of the boundary layer. This can introduce a significant error for ultra-low Reynolds numbers. Under these conditions the pressure is not necessarily constant through the boundary layer. The variation in pressure coefficient through the boundary layer is shown in Figure 6 for the upper surface 50% chord location of a NACA 4402. The section is operating at one degree angle of attack and Re 1000. There is variation of 18% in the pressure coefficient between the surface of the airfoil and the outer edge of the boundary layer. The outer edge of the boundary layer is defined as the location of maximum velocity along the normal to the surface. This variation will be related to the thickness of the boundary layer, with less variation forward of this station and more aft, but it is clearly non-zero. Neglecting this variation introduces an error in both lift and drag calculations.

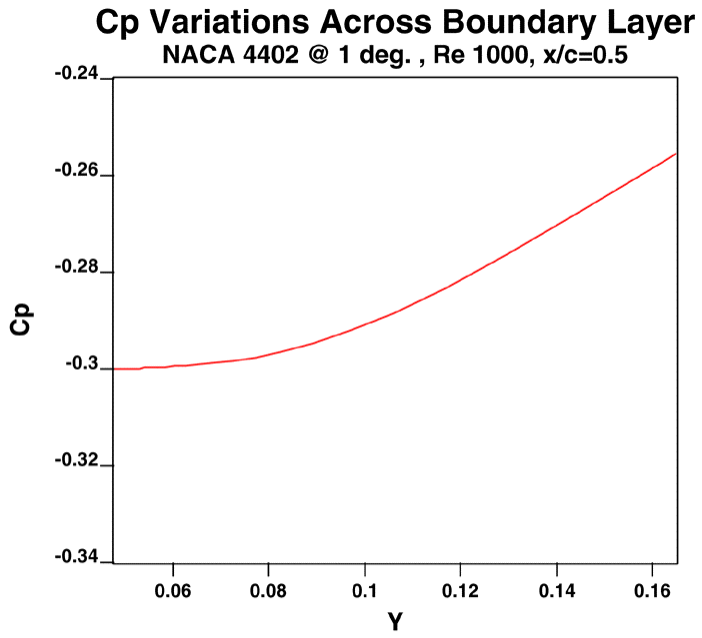

Figure 6. Variation of pressure through the boundary layer.

Considering the added complexity and computational effort required for the Navier-Stokes solution, MSES performs very well over its much smaller range of convergence. It is the inability to converge at higher angle of attack that firmly establishes the need for a higher fidelity solver, capable of dealing with the large regions of separation that form. Reaching only 50 % of maximum lift and 65% of the maximum lift to drag ratio is inadequate. Although the lift and drag of the simpler method agrees well with the Navier-Stokes solution at low lift coefficients, the operational requirements of this very small flight vehicle necessitates maximizing the performance of the airfoil section.

3.2.4 General Performance Characteristics of Airfoils at Ultra-Low Reynolds Numbers:

The primary goal of this work has been to establish the effects of section camber, thickness, and operational Reynolds number on two-dimensional airfoils. All sections are members of the NACA 4-digit family. All analyses utilized the INS2D flow solver. All solutions are steady state and fully laminar. The steady state assumption is supported by the adequate convergence histories of the flow solutions. The fully laminar assumption is reasonable and in fact necessary at the ultra-low Reynolds numbers, 20,000 and lower, being considered. Imposing a transition location would likely be an artificial mechanism that could not be physically realized. Even if sufficiently large artificial trips could be implemented without causing complete laminar separation, it is likely that the transition length would exceed the chord of the airfoil.

3.2.4.1 Basic Camber and Thickness Effects:

The initial analyses considered the general effects of camber and thickness at a Re 1000. Three sections were considered: NACA 0002, 4402, and 4404. The resulting drag polars are provided in Figure 7. Prior to this analysis is was unclear if the overall effect of camber would be the same at very low Reynolds numbers. It was thought that the decambering effect of the considerably thicker boundary layers might effectively wash out the camber completely. The INS2D results for the 0002 and the 4402 demonstrate that camber is still a very effective parameter. The 4% cambered section

exhibits the expected upward shift, providing lower drag at higher lift coefficients, but the addition of camber also significantly increases the predicted C_{lmax} of the section from 0.55 to 0.74. These two effects combine to increase the maximum lift to drag ratio from 4.5 to 5.5. The C_l for maximum L/D also increases from 0.54 to 0.71. The effect of section thickness on drag is also visible in Figure 7. The increase in thickness from 2% to 4% results in a 15% drag penalty around maximum L/D and a similar reduction in the magnitude of the maximum L/D.

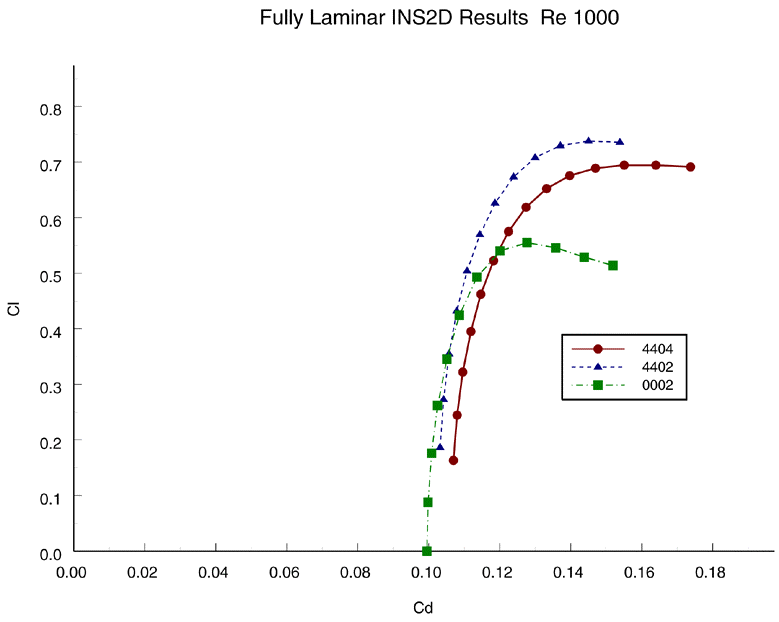

Figure 7. Drag polars for sections with various camber and thickness.

3.2.4.2. Reynolds Number and Additional Thickness Effects:

Using the 4402 and 4404 sections, additional runs were completed to explore the effect of Reynolds number variations and to gain further insight into thickness effects.

The lift curves and drag polars for the two sections over a range of Reynolds numbers are provided in Figure 8 and Figure 9. The lift curves show the general trend of increasing C_{lmax} with decreasing Reynolds number. This may seem counter intuitive, but the flow field appears to become much less susceptible to the onset of unsteady separated flow with decreasing Reynolds number. Lower Reynolds number implies a reduction in the ratio of inertial to viscous effects in the flow field. The increase in the viscous effects can be seen in Figure 9 as the substantial increase in drag with decreasing Reynolds number. The effect of the reduction in the inertial effects is seen in the increase in C_{lmax}. As Reynolds number is decreased, large stable eddies develop on the upper surface of the airfoil. The inertially damped flow field is less likely to separate catastrophically and exhibit unsteady behavior.

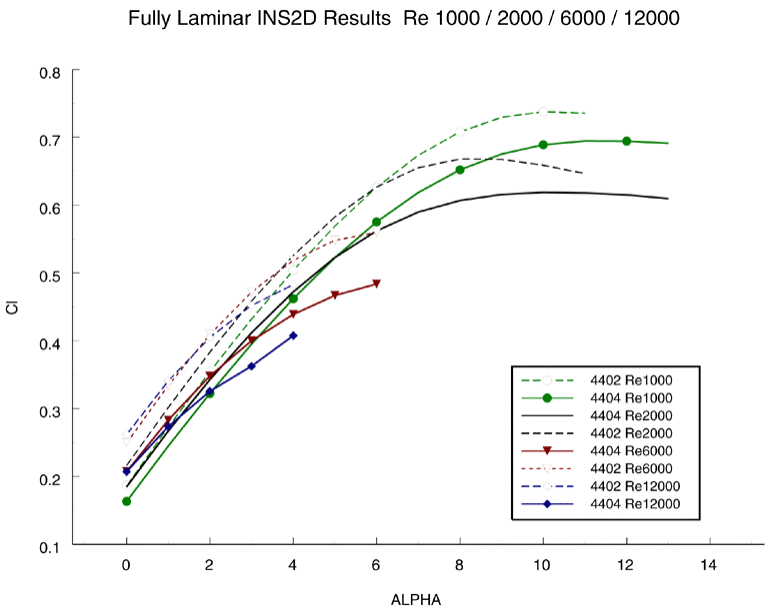

Figure 8. Variation of lift coefficient with angle of attack over a range of Reynolds number.

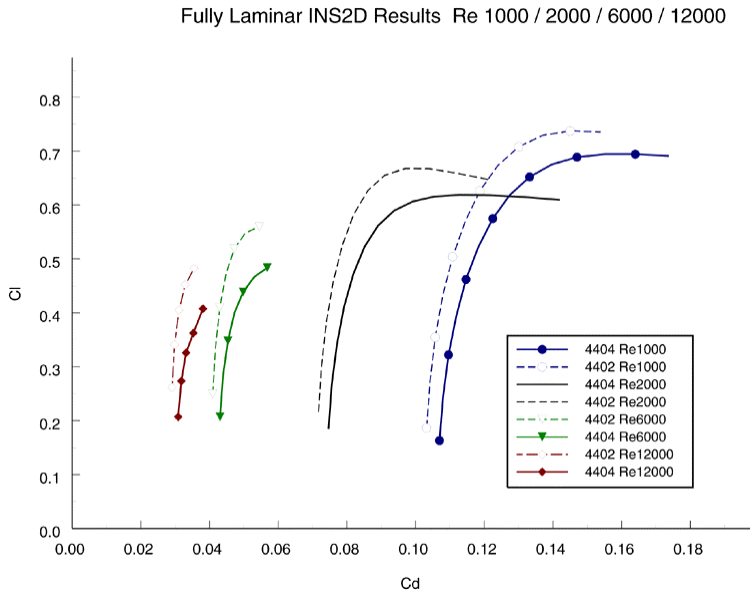

Figure 9. Drag polars for sections with varying thickness.

This lift behavior is opposite, and the drag behavior is consistent, with what is seen as normal behavior for airfoils as Reynolds number is decreased from high values down below 100,000. In this regime, the increase in the viscous effects, the increase in boundary layer thickness, etc., must be more destabilizing then the reduction in inertial effects is stabilizing. Then at some point above the range of Re considered here, there is a crossover, and the reduction in flow inertia begins to win out, delaying the onset of unsteady separation and increasing the maximum section lift coefficient.

The trends in C_{lmax} and maximum L/D for the 4402 and 4404 are provided in Figure 10. As the Reynolds number approaches zero, the C_{lmax} increases from rather low values towards values

approaching one. The C_{lmax} recovers to a value quite similar to those generally attainable for Reynolds numbers of order 100,000 and greater. The increase in lift does not compensate for the rapid increase in drag when considering L/D , but even as the Re approaches zero maximum L/D stays well above one, approaching 2.5 in the limit. Similar trends have been observed in limited experimental data utilizing a 14% thick airfoil [6]. This experiment found maximum lift coefficients in the range of 0.8 to 0.5 in the Reynolds number range of 100 to 1000. The reported drag is substantially higher, but this is likely due to the large increase in section thickness.

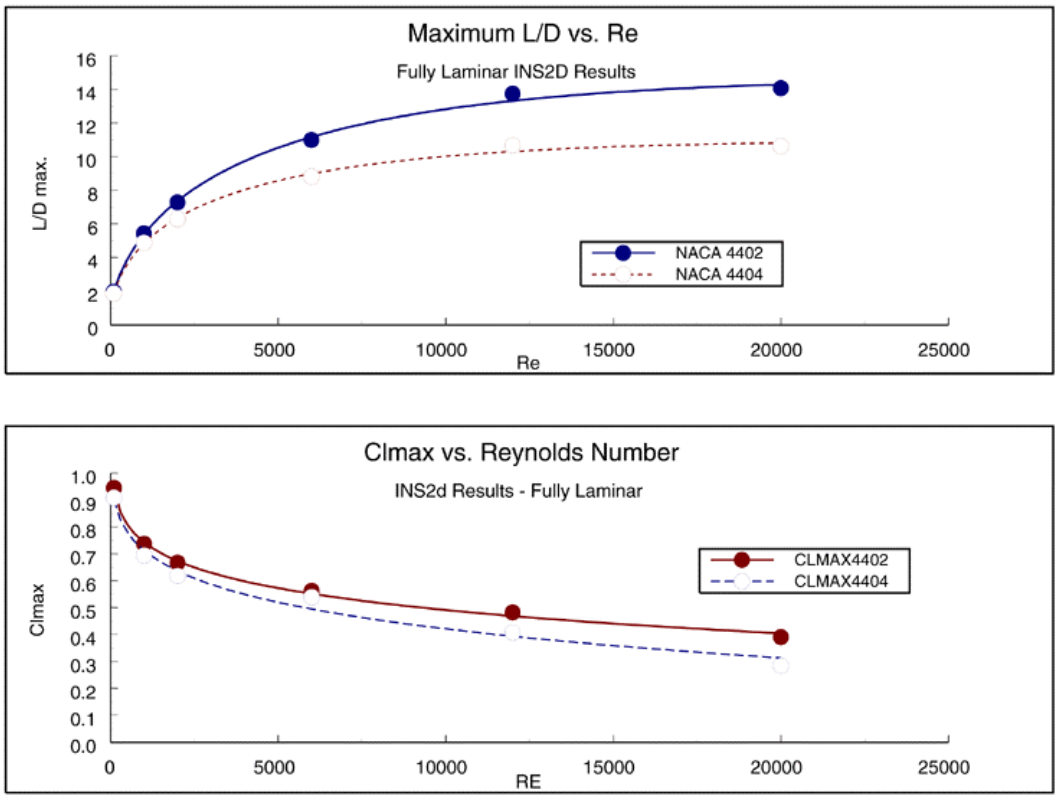

Figure 10: C_{lmax} and maximum L/D vs. Reynolds number

The trends depicted in Figure 10 may appear erroneous in that the maximum L/D appears to asymptotically approach values between 10 and 14. Typical sections at much higher Reynolds numbers exhibit values of order 100. The reason for the plotted behavior is that the thin, relatively sharp-nosed sections, become less efficient as the Reynolds number is increased. At the Reynolds numbers being considered, small magnitude changes correspond to substantial changes in the behavior of the flow field. In order to see the expected trend, a series of different sections, each optimized for a small range of operation, would have to be superimposed.

Also visible in Figure 8 and Figure 9 is a lateral and upward shift of the lift curve and drag polar with decreasing section thickness. This effect is similar to that associated with an increase in camber. The increased thickness of the 4404 section appears to increase the decambering effect of the boundary layer.

3.2.4.3 Parametric Study of Camberline Variations:

The previous results have shown that section geometry variations have a considerable effect on section performance. Previous analyses considered only one camber location and magnitude. In an attempt to further improve section performance and explore the value of a detailed design effort, a nine point parametric study of section performance has been completed. The varied parameters are the camber magnitude and the chordwise location of maximum camber. All sections are 2% thick with an NACA 4-digit camberline and thickness distribution. All sections were analyzed at Re 12,000. The test points and a summary of the results are shown in Figure 11.

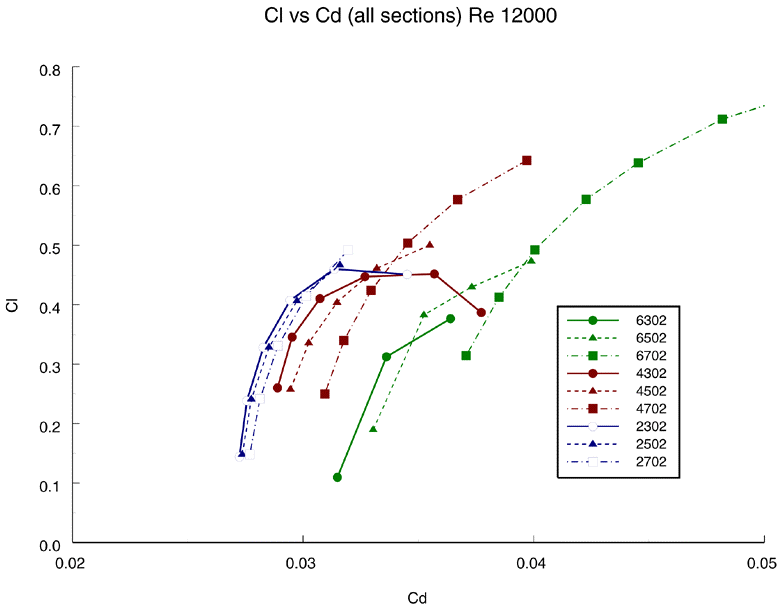

Figure 11. Effect of section camber on drag polars at low Reynolds number.

The performance of the sections varies considerably from point to point, supporting the premise that detailed section geometry design is a worthwhile endeavor. Somewhere within the design space exists at least one optimal design. The substantial variations in performance across the test matrix imply that an optimal design may offer significant performance gains over the limited number of sections considered thus far.

The only trend visible in the results is a performance advantage in conjunction with an aft shift in the maximum camber location. For this limited test matrix, the 4702 section exhibits the best performance in terms of high maximum L/D occurring at a high lift coefficient. This section will likely be implemented in the next iteration of rotor design, replacing the current 4402. Figure 12 incorporates the 4702 drag polars with those of the 4402 and 4404 for several Reynolds numbers. The much higher C_{lmax} of the section results in considerable gains in L/D, but the stall characteristics of the section at the higher Reynolds numbers appear to be more abrupt and less forgiving. In application, it would be prudent to back away somewhat from the maximum L/D in order to provide some stall margin.

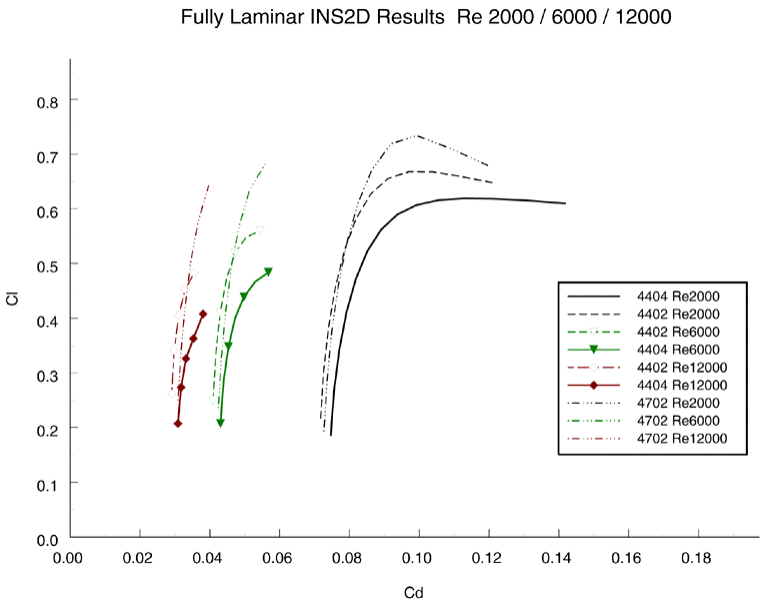

Figure 12. Effect of camber, thickness, and Reynolds number on drag polars.

3.2.4.4 Three Dimensional Rotor Analysis and Optimization

Data from the 2D Navier-Stokes analysis was represented by a simple 2-D regression model and incorporated into a three dimensional rotor analysis and design code. This program uses basic vortex and momentum theories combined with stripwise viscous corrections to compute rotor thrust and torque at a specified rotation rate. Hub and tip corrections and the effect of slipstream swirl are also included. This program was coupled with a nonlinear optimizer and a fit of our electric motor performance map in order to optimize blade chord and twist distributions, RPM, and rotor diameter. The number of blades was varied parametrically. Further details on the rotor optimization are available in the final report, but the optimized rotor geometry, shown in figure 13 was derived and estimated to be able to achieve as much as 1g of static thrust per rotor with the 3mm RMB micro-motors. Subsequent experiments showed that at the specified RPM our rotors achieved about 80% of this value, an acceptable agreement, but with some uncertainty as to the actual torque required. These tests are summarized in section 3.3.2. Next we describe rotor fabrication steps and materials considerations.

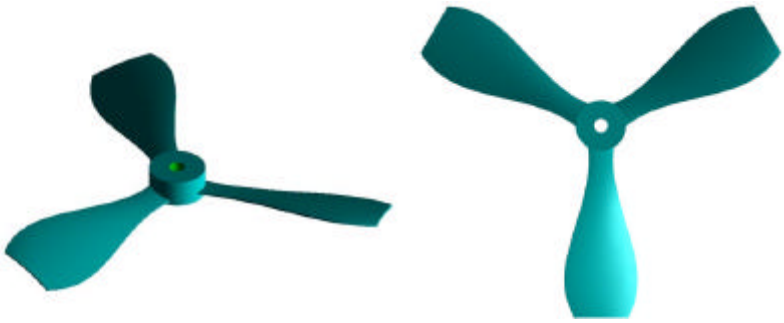

Figure 13. Geometry for 1.5cm rotor developed by optimization.

3.3 Manufacturing and Testing

3.3.1 Rotor Material Selection and Manufacturing Method

According to design specifications rotor blades have to be thin 3-dimensional structures, with minimum strength and stiffness properties for operation and handling. Three material categories were considered: polymers, metals, and ceramics. A variety of manufacturing processes for these material categories are compared in the following table. SDM refers to 'Shape Deposition Manufacturing' a sequence of additive and subtractive processing steps for the fabrication of complex 3D parts. Mold SDM is a variation of this process for the creation of complex shaped fugitive wax molds. A spectrum of castable polymer and ceramic materials have been used to make parts from these molds. [7]

Material	**Polymer**	**Metal**	**Ceramics**
Manufacturing Method	SDM or Mold SDM Wax as substrate Cast polymer as the part material	Sputter metal onto wax substrate electroplate propeller material	Mold SDM Cast ceramics slurry to obtain green parts, which can be sintered
Characteristics	3D thin blades with non uniform thickness if required	Produces blades with uniform thickness Metals or alloys that can be electroplated	Need entire mold instead of substrate only
Advantages	Produces blades with non uniform thickness Simple process Shaft can be attached during casting	Produces very thin structures Electroplating process suitable for mass production	Light weight and stiff structures
Disadvantages	Achievable thickness limited by material properties	Metals ductile Sputtering time consuming Non-uniform thickness difficult	Slow process Green parts fragile Shrinkage and warpage during sintering

From this preliminary analysis, polymers are considered the top choice for rotor prototypes. Three different polymers are compared in the subsequent section.

Considering materials and manufacturing constraints, SDM of polymers has been found to be a suitable process for rotor fabrication. A detailed sequence of manufacturing steps is illustrated in the following:

Figure 14. Rotor fabrication steps 1 to 5

- *CAD modeling based on the design parameters:* Chord length, twist angle and cross-section shapes are given at 25%, 50%, 75%, and 100% of the radius. Due to the manufacturing and strength considerations, the parts close to the center hub should be modified to avoid weak connections and stress concentration.
- *CNC code generation:* After model is created, CNC machining code is generated through a commercial CAD/CAM package.
- *Substrate preparation:* Support material is machined to obtain the geometry of bottom surface of rotor by 3-axis CNC mill. (step 1)
- *Polymer casting.* Part material, i.e.polymer, is cast to fill cavity. (step 2)
- *Surface flattening:* Remove excess polymer on top of wax surface. (step 3)
- *Material shaping to net shape.* CNC machine geometry of top rotor surface. (step 4)
- *Substrate removal.* If the rotors cannot be pulled out of the substrate directly, wax should be melted at 150 degrees C, remaining traces can be removed with BioAct. (step 5)

Since CNC milling plays an important role in shaping the rotors, availability of appropriate end mills and machine accuracy are considered crucial for success. The smallest available ball end mills are 0.254 mm with a flute length of 0.762 mm. Feasible machining strategies are subject to these constraints. In addition, resolution of CNC cutting steps was chosen as one micron. Surface quality mainly depends on the magnitude of chosen cutting steps. While tool wear is normally an important issue at this scale, wax and polymer materials are soft and therefore easy to machine without significant tool wear.

Three polymers were used to build rotors in the first 6 months, Adtech EE-501/530 Epoxy, Adtech LUC 4180 Polyurethane, and Ciba TDT 205-3 Polyurethane. These three materials were investigated and characterized in previous SDM research [8]. All of them can be cast and cured at room temperature, furthermore they are easy to machine by a 3-axis CNC mill with carbide ball end mills. The following table compares material properties of these three materials:

Material	Adtech EE-501/ 503 Epoxy	Adtech LUC 4180 Polyurethane	Ciba TDT 205-3 Polyurethane
Ultimate tensile strength (MPa)	42	55	23
Elogation to failure	1%	15%	9%
Hardness (Shore D Scale)	86-89	78-80	70
Cure time before machining	24 hours	12 hours	2 hours
Bonding to wax	good	good	weak
Machinability	good	good	good
Comments	Very brittle Long cure time Wax substrate must be melted away at the end and can not be reused.	Too soft to retain 3D geometry High tensile strength Long cure time Can be removed from wax substrate directly, subtrate can be reused	Low tensile strength short cure time Can be removed from wax substrate directly, substrates can be reused.

3.3.2 Lift Test

Lift tests of rotor blades were conducted by a pendulum setup a shown in Figure 15. A 3 millimeter diameter micro motor, made by RMB miniature bearings, Inc., was used to power propellers. During testing, horizontal deflections of pendulum were measured at different motor frequencies Deflections were used to calculate motor thrust and compare with the computational estimates.

The effect of the following propeller parameters was investigated: Rotor diameter, number of blades, pitch angle of the blades, and the shape of the leading edges of the blades.

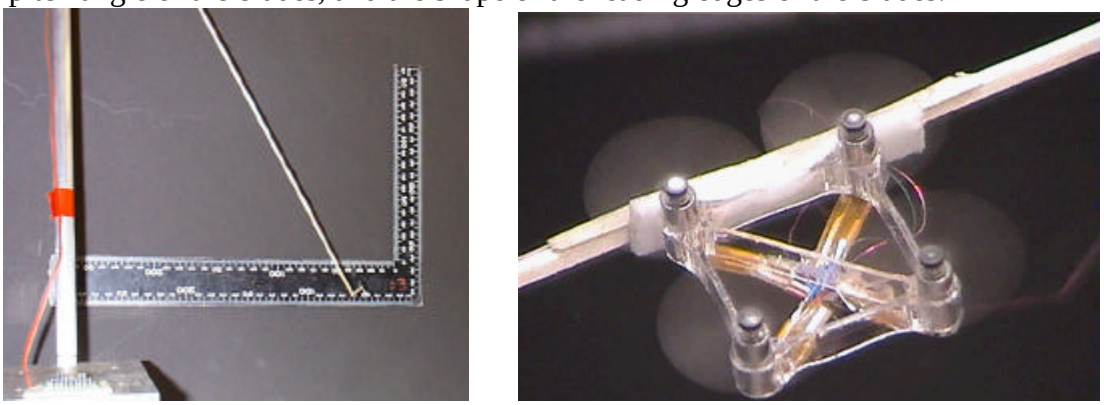

Figure 15. Single rotor lift test (left) and 4-rotor constrained mesicopter test (right).

Rotor diameter

Two sets of rotors, 15mm and 30 mm in diameter, were built to study how size affects lift and drag. The larger rotor stalled motor at one-forth frequency of small rotor. However, maximum lifts generated before stall are similar.

Figure 16. 15 mm and 30 mm rotor models

Number of blades

15 mm diameter rotors with 2, 3, and 4 blades were built and tested to measure dependency of number of blades on performance. Results suggest that additional blades increase both lift and drag at a given frequency at the same rate and no extra lift can be gained by adding more blades.

Figure 17. Rotors with different blade counts

Pitch angle of the blades

The effect of different pitch angles of the blades was investigated. Based on the optimal design, propellers were built with pitch angles increased by 2 and 4 degerees.

Higher pitch angles resulted in higher lifts, however, the effect was much weaker than predicted by numerical models.

Leading edge design of blades

A set of rotors was built with the leading edge of the blades rounded to investigate the effect of the leading edge geometry on aerodynamic performance. Different leading edge geometries did not affect the stall frequency and maximum lift. However, rounded corners did improve stability of the rotor.

3.3.3 Micro Motor

3.3.3.1 Design objectives

In order to satisfy the high performance requirements of the mesicopter application a permanent magnet excited stepper motor design was chosen. This type of motor offers much higher power output than similarly sized electrostatic stepper motors but does not suffer from the poor scaling characteristics of magnetic field based variable reluctance motors. It does, however, impose strong demands on the materials used and only few processes have been found that can shape meso scale parts out of the materials required, especially hard and soft magnetic alloys.

3.3.3.2 Principle of operation

The motor design is shown in Figure 18. It has four stator poles and two rotor poles. Instead of coils, which are very difficult to fabricate in the small scale, a simple copper structure is used that forms single turn coils. If the current is switched like four phase alternating current, a rotating magnetic field is created inside the stator structure. The hard magnetic rotor will try to align itself with the external magnetic field and will therefore rotate synchronously with the stator field.

Since the design does not require coils, it is expected to be very suitable for economical mass fabrication in the meso scale size range. The power output and efficiency should be comparable to a similarly sized motor that does have coils. Due to its single turn armature coils the impedance of this motor will be very low, i.e. it will require high current at low voltages. This problem can be overcome if the motor controller is placed right next to the motor and also works as an impedance converter (like a switched power supply).

Figure 18. Exploded view of micro motor

3.3.3.3 Simulation efforts

Initial efforts were taken to numerically analyze the motor design. Unlike electrostatic micro motors or variable reluctance motors the motors used for this project have a significant holding torque, i.e. they will not spin freely if no electrical current is supplied. Due to magnetic attraction the rotor tries to align its poles with the soft magnetic stator poles, and the armature current has

to be strong enough to overcome this torque. In fact, the torque generated by the armature coils should be much stronger than the holding torque, otherwise the output torque will pulsate several times on each revolution of the rotor.

While a motor can be designed without the soft magnetic stator, thereby avoiding the problems with the holding torque, motors with soft magnetic stators are expected to show much higher output performance. In order to avoid lengthy prototyping cycles and experiments, a simple model of the motor configuration was developed and the magnetic field inside the motor was calculated for different stator geometries.

3.3.3.5 Manufacturing techniques

Objectives

The particular motor design imposes strong requirements on material properties. While most micro shaping techniques are limited to silicon, copper, and nickel, the motor needs hard and soft magnetic structures to operate, and hard materials are required for low friction bearings. Shaping techniques for quick prototyping and for mass production had to be developed to create parts made from the required materials.

Magnetic materials are hard to shape, because they can not be deposited. Their crystalline structure has a large impact on their performance, and deposition techniques that can achieve the necessary deposition rates, like electro plating or PVD, allow no control over the resulting micro structure. Photo lithography and anisotropic etching on the other side are restricted to the few materials allowed in a clean room environment.

Manufacturing concept

Most micro fabrication techniques can not directly shape magnetic materials, whereas most large scale shaping techniques for these materials can not easily be used for micro- and meso scale structures. A novel fabrication technique was needed that could create the precise and fine featured geometries commonly obtained by micro machining out of engineering materials. One factor that has traditionally limited the feature resolution of large scale shaping techniques was that the tools had to be at least as small and as accurate as the smallest features of the part.

The fabrication setup developed at the Rapid Prototyping Laboratory at the Stanford University attempts to use common micro fabrication techniques like LIGA or silicon processing to create the tools that are then used to shape the final part material. Most of these tools are destroyed in the final shaping process and can not be reused. However, since most micro fabrication techniques can produce patterns in a highly parallelized fashion, the actual tool cost is low. To create quick prototypes, a fine pattern can be created in wax, and then transferred into the final part material. Machinable wax causes almost no tool wear, therefore even tiny cutting tools can be used efficiently.

The research work focused mainly on finding and characterizing shape transfer techniques from silicon and wax into polymers, metals, ceramics and both soft and hard magnetic materials. A number of different pattern transfer techniques were found for each class of materials:

- polymer: casting, hot embossing
- ceramics: gel casting
- metals: electro plating, electro discharge machining, gel casting
- magnetic materials: electro discharge machining, casting of powder filled polymer

Fabrication of motor parts

A variety of techniques were used to fabricate the individual pieces of the micro motor. The main considerations for the choice of technique were part geometry, part material, required accuracy and potential for parallelization.

Armature coils

The armature coils have to be made out of material with excellent electrical conductivity, like copper or silver. Electro plating can fill in tiny cavities and has therefore been chosen to create the copper structures used in the motor. The process sequence works as follows:

- Holes are etched into a silicon wafer with a commercial plasma etcher
- A copper seed layer is sputtered onto the wafer with the ring shaped holes.
- A wafer with ring shaped holes is stacked onto a wafer with through holes (Figure 19)
- The stack is attached to the cathode of a copper electro plating bath.
- After the cavities are completely filled in the stack is removed from the electro plating bath, the top side is polished flat to remove excessive copper deposits.
- Finally the silicon mold is etched away in boiling KOH solution.

Figure 19. Stacked wafer mold

Rotor

The rotor has to be made out of hard magnetic material. There is no easy way to deposit hard magnetic materials, therefore the fabrication process must shape stock materials. Two methods have been used so far: EDM of NdFeB and casting of NdFeB powder in a polymer binder.

The EDM electrodes were made by electro plating copper into a silicon cavity, then soldering the structure onto a copper block and removing the silicon. Since, according to experiments conducted in our lab, magnets can be EDM-ed in the magnetized state, complex magnetic configurations can be assembled from larger magnet pieces and then patterned with fine featured electrodes. This allows fabrication of small magnetic structures which are not just linearly magnetized but can have arbitrary magnetization patterns (e.g. a quadrupole field).

Casting of powder and polymer binder makes the mold removal more challenging, since many silicon etchants will attack polymers, too. Also, the resulting structures are much weaker magnets than pure NdFeB structures. However, unlike EDM, casting is a highly parallelizable process and therefore much more suitable for mass production. For quick prototyping of cast magnetic structures a wax mold can be used instead of a silicon mold.

Stator

The stator consists of soft magnetic material and guides the magnetic field around the armature coils to the rotor. Like in the case of the rotor, both EDM and powder casting can be used to create the structures.

EDM was used to pattern thin sheets of amorphous metal. Several of these patterns would be stacked to form a stator. This laminated setup allows the structure to operate at the higher frequencies common in micro actuators without sacrificing permeability.

The powder, cast together with a polymer binder would yield structures with relatively low permeability (μ relative of up to 18 was achieved), but good insulation properties, and the ability to operate at much higher frequencies and again, the ability to easily mass fabricate soft magnetic structures.

Micro motors built at the RPL: First working model

The first working micro motor built in the RPL consisted of an armature coil and a ring shaped rotor in the center, held in place by a tungsten shaft (see Figure 20). The absence of a soft magnetic stator reduced the performance but the main goal of this design was to get experimental data that could be used to verify the simulation results. Also, issues like friction related problems would become apparent at this stage and could be addressed in future designs.

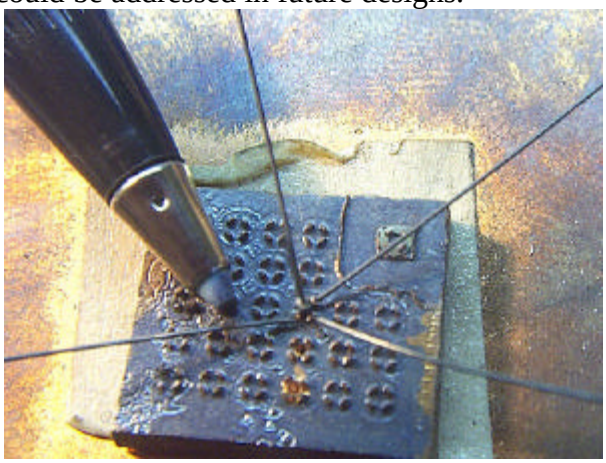

Figure 20. Micro Motor Developed at RPL

An optical speed measurement device was designed and built to verify that the motor indeed spun synchronously with the electrical pulses. A fiber optic would shine IR light on the rotor, which had copper sputtered on one half of its top surface. A second fiber optic, aimed at the same spot on the rotor, would pick up the reflected IR light and guide it to a pin diode. With this setup a maximum motor speed of 10000 rpm was measured, with a drive current of 2 A per pole.

The biggest problem with this design was the fact, that there had to be a large gap between the rotor and the shaft to account for thermal expansion and tiny particles broken loose from the rotor that could potentially seize up the motor. Due to this large gap the rotor would tend to wobble as it spun. While this was not a serious problem in this setup, it would have bad consequences on a motor with a soft magnetic stator, where it is important that the rotor is centered so it sees only torque but no net force from the stator.

Motor with jewel bearing

Based on the experiences gathered with the initial design a second type of micro motor was designed and built. Instead of a tungsten shaft going through the rotor the whole rotor is now glued onto an alumina shaft, which is held in place by a jewel bearing setup (see Figure 21). The armature structure is then placed around the rotor and connected to the power source.

Figure 21: Experimental jewel bearing setup

With this setup a nearly vibration free motion of the rotor could be achieved, which allows experiments with different soft magnetic stator designs. Additionally, since the rotor sticks out freely on the top side, it is much easier now to attach loads to it for measuring the output torque of the motor.

3.3.4 Power Sources

Design Considerations

To date, all power-related work has focused on powering the motor currently in use, the 3mm micro motor made by RMB miniature bearings, Inc. Due to the major expenditures required for custom-built batteries utilizing current production technologies, commercially available battery chemistries have been pursued, specifically zinc-air, silver oxide, alkaline, and lithium-manganese dioxide.

Power Requirements

Battery testing for the first prototype has focused on supplying enough power to the motors to enable liftoff and short-duration flight. Although the micro motors nominally draw 35mA, tests at the RPL have indicated the motors can be safely operated at up to 50mA for extended periods of time. For the rotors tested thus far, currents near 45-50mA are needed in order to generate sufficient rotor speed. Consequently, battery testing has been carried out aiming to supply 50mA per motor. The battery combination must supply the minimum voltage (3 volts) needed for operating the motor controller. The drain rates required are quite high for commercially-available battery technologies at the light weights required.

Performance Comparison

Alkaline, lithium, silver oxide, and zinc-air chemistries were considered and tested. Alkaline batteries were in general found to be capable of delivering nearly enough current, but were not available in the weight range necessary for the mesicopter. Zinc-air cells are unable to supply the requisite current for more than a few seconds. Lithium batteries we tested were generally unable to support the drain rates the mesicopter required. However, recent developments in this field may make lithium based batteries more attractive shortly. A class of high-drain silver oxide cells showed the greatest potential. The results of the most promising existing cells are summarized below.

Battery Model	**Chemistry**	**Rated Capacity (mAh)**	**# tested in series**	**Voltage (V)**	**Current (mA)**	**# batteries needed for 4 motors**	**Mass (g) of one battery**	**Battery mass per motor (g)**	**Power density (mW/gram)**
Energizer 2L76	*$LiMnO_2$*	*190*	*2*	*4.1*	*180*	*2*	*6.0*	*1.5*	*123*
Rayovac 361	*Silver Oxide*	*23*	*3*	*3.132*	*50*	*12*	*0.42*	*1.26*	*124*
Rayovac 389	Silver Oxide	85	3	3.1	100	6	1.21	1.82	85

From the chart above emerge three promising batteries: the Energizer 2L76, the Rayovac 361, and the Rayovac 389. The Energizer 2L76 is a lithium manganese dioxide cell designed for use in high-drain applications such as driving a photo flash. The silver oxide cells tested are also high-drain cells. The 2L76 is the heaviest battery at 1.5 grams per motor, and requires only two batteries connected in series. The Rayovac cells offer similar power densities at about 0.25 grams less (per motor). The major difference between the two Rayovac options is the size and number of batteries required. The 361 would require 12 batteries, while the 389 combination requires only four batteries. During prototype testing, the most promising batteries have been mass-reduced by grinding and sanding. This has made it possible to achieve "battery mass per motor" levels just under 1 gram for both the Rayovac 389 and Rayovac 361. Subsequent work will include new lithium polymer batteries from SRI and 30mAH NiCd cells which were obtained only at the end of Phase I.

3.4 Additional Considerations in Phase I Work

Our primary emphasis in Phase I was on the aerodynamics and manufacturing of the first mesicopter prototype. However, during this time, preliminary work was also undertaken to understand some of the stability and control issues, flight control sensing requirements, and potential issues associated with payload communications requirements. As part of this work we travelled to Pasadena and discussed some of these issues with researchers from Cal Tech and JPL and have had a number of discussions with colleagues at SRI and Intel. The results of this concept-level research is described in the Phase II proposal.

4. Conclusions and Future Work

Results of the Phase I work, including computational and expermiental studies, suggest that free-flying mesicopters in the 1-10 centimeter scale are indeed feasible. Our proposal for subsequent research contains additional information on the mesicopter concept and the applications we envision. The objectives of the second phase of work proposed in this program include the following:

- Designing and building a remotely-commanded centimeter-size flight vehicle capable of carrying its own power supply.
- Designing and testing control strategies for remote control of a single mesicopter.
- Developing fabrication methods suitable for fabricating arrays of mesicopters in an economic fashion.
- Designing and integrating power systems, which enable mission times of tens of minutes.
- Demonstrating feasibility of mesicopter system.
- Investigating the underlying science and technology concepts to enable coordinated flight of large numbers of mesicopters.
- Further exploring of mesicopter system roles in the context of NASA missions.

5. Additional Information

For further insight into our research on mesoscale flight vehicles please visit: http://www.aero.stanford/mesicopter/
This site includes numerous additional images and video clips of our first constrained flights.

or contact :

Prof. Ilan Kroo	(650) 723-2994
Dept. of Aero/Astro	(650) 725-3314 (FAX)
Stanford University	kroo@stanford.edu
Stanford, CA 94305	http://aero.stanford.edu
Prof. Fritz B. Prinz	(650) 723 0088
Depts of Mechanical Engineering and Materials Science and Engineering	(650)723 5034 (FAX)
Stanford University	fbp@cdr.stanford.edu
Stanford, CA 94305	http://www-rpl.stanford.edu

6. References

1. N. Miki, I Shimoyama, "Analysis of the Flight Performance of Small Magnetic Rotating Wings for Use in Microrobots", Proc. 1998 IEEE International Conf. on Robotics and Automation, Leuven, Belgium, May 1998.

2. Martinelli, L., Jameson, A., "Validation of a Multigrid Method for the Reynolds Averaged Equations," AIAA Paper 88-0414, AIAA 26th Aerospace Sciences Meeting, Reno, NV, January 1988.

3. Rogers, S. E., Kwak, D., "An Upwind Differencing Scheme for the Time Accurate Incompressible Navier-Stokes Equations," AIAA Paper 88-2583, June 1988.

4. Drela, M., Giles, M. B., "ISES - A Two-Dimensional Viscous Aerodynamic Design and Analysis Code," AIAA Paper 87-0424, AIAA 25th Aerospace Sciences Meeting, Reno, NV, January 1987.

5. Drela, M., "XFOIL – An Analysis and Design Program for Low Reynolds Number Airfoils," Low Reynolds number aerodynamics; Proceedings of the Conference, Notre Dame, IN, June 1989, Springer-Verlag, Berlin and New York, 1989, p. 1-12.

5. Eppler, R., Somers, D. M., "A Computer Program for the Design and Analysis of Low-Speed Airfoils," NASA-TM-80210, August 1980.

6. Thom, A., Swart, P., "The Forces on an Aerofoil at Very Low Speeds," Journal of the Royal Aeronautical Society, Vol. 44, pp. 761-770, 1940.]

7. A.G. Cooper, S. Kang, J. W. Kietzman, F. B. Prinz, J. L. Lombardi and L. Weiss, "Automated Fabrication of Complex Molded Parts Using Mold SDM" (PDF, 205k), *Proceedings of the Solid Freeform Fabrication Symposium*, University of Texas at Austin, Austin, Texas, August 1998.

8. J. W. Kietzman and F. B. Prinz, "Material Strength in Polymer Shape Deposition Manufacturing" (PDF, 53k), *Proceedings of the Solid Freeform Fabrication Symposium*, University of Texas at Austin, Austin, Texas, August 1998.